ATLAS

P. Albicocco(Ass. Tecn.), M. Antonelli(Resp.), C. Arcangeletti (dott.),
M.M. Beretta, H. Bilokon, E. Capitolo(Tech.), G. Ceccarelli(Tech.),
S. Cerioni(Tech.),V. Chiarella, M. Curatolo,
E. Dane', G. Delle Monache, M. Dreucci,
B. Esposito, G. Ermini(Tech.), G. Fontana(Tech.),
C. Marini(Tech.), M. Gatta(Tech.),
P.F. Laurelli, S. Lauciani(Tech.),
G. Maccarrone, A. Martini, G. Mancini(Ass. Ric.),
D. Orecchini(Tech.), M. Paris (Tech.), G. Pileggi (Tech.),
B. Ponzio(Tech.), F. Putin(Tech.),
V. Russo(Tech.), A. Sansoni, F. Sborzacchi(Tech.),
M. Testa, S. Tomassini, P. T. Vassilieva(Tech.), E. Vilucchi.

In collaboration with:
Centro di Calcolo:
M. Pistoni, D. Spigone

February 27, 2020

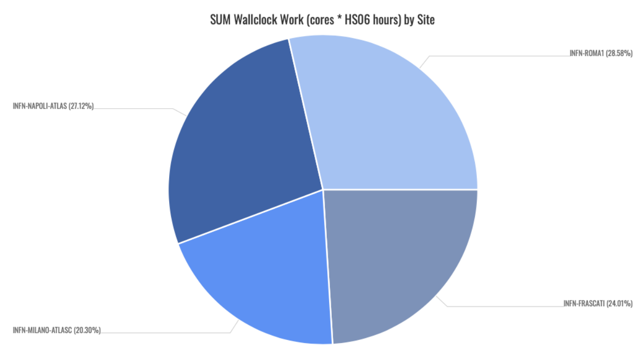

Figure 1: SUM of wall-clock work for ATLAS VO

1 Introduction

In the 2015-2018 data taking ATLAS collected proton-proton collisions at 13 TeV center of mass energy corresponding to an integrated luminosity of about 147 fb^{-1}.
Our group contributed significantly to the analysis $H \to ZZ \to 4\ell$ as will be described in the following.
These contributions have been made possible also thanks to the reliability and the tools available on the LNF Tier2 approved by the INFN.
In parallel with the data taking activity, including shifts and maintenance, we are deeply involved in the new Small Wheel for the Phase I upgrade of the muon system. We are also strongly involved in the design and construction of the new Inner Tracker (ITk) for the Phase II upgrade. For the Phase II we also contributed significantly in the improvement of the jet performances using tracking information.

2 Tier-2

During the year 2019 the Frascati Tier2 successfully and continuously performed all the typical activities of an ATLAS Tier-2: Monte Carlo production and users and physics groups analysis. The PADME experiment consolidated its activity on the Tier-2 farm storing raw, MC and reconstructed data in the storage system and running MC, reprocessing and analysis jobs in the Tier2 cluster, with pledged resources. During the year, the Tier-2 farm has reached 38 kHEPSPEC of computing power and about 2.4 PB of disk space, running also the computing activities of the following Virtual Organisations (VO): LHCb, Belle, CTA and KM3Net.
In Figure 1 the sum of wall-clock work (cores * HS06 hours) by site for the ATLAS Italian Tier-2's sites.
Among the activities that involved the Tier-2 staff we mention the role of VO

manager for ATLAS VO (recognised as in kind contribution of the Italian group) and software VO manager for KM3Net VO.
For what concern the Grid middleware, during 2019 the Tier-2 staff continued to test and develop the cache systems, with the DPM storage system, in collaboration with the Italian ATLAS Tier-2 federation staff and as part of the IDDLS (Italian Distributed Data Lake for Science) project. Moreover, the IBiSCo computer PON has been approved for three years and the acquisitions of the first hardware resources is started: six servers.

3 New Small Wheel upgrade project: Micromegas [7] [8]

MicroMegas (MM) chambers is an abbreviation for MICRO MEsh GASeous Structure and it is an innovative design concept for Micro-Pattern Gaseous Detectors first introduced by Charpak and Giomataris during the 1990s. These chambers have been chosen as new precision tracking detectors for the upgrade of the forward muon spectrometer of the ATLAS experiment at the Large Hadron Collider (LHC) during the second long shut-down of the LHC [9].
MicroMegas are gas detectors in which a 5 mm gap between two parallel electrodes is filled with a 93 : 7 $Ar : CO_2$ gas mixture and a thin metallic micromesh is placed between the two electrodes, held by pillars with a pitch of few millimeters and a height of about 128 μm. The drift electrode, with a -300 V voltage applied, and the mesh, which is grounded, define the drift region, where the ionisation takes place and the low electric field ($\sim$600V/cm) leads the produced electrons towards the mesh. Following the field lines the electrons enter the very thin amplification region between the mesh and the readout electrode, which is segmented into strips with a pitch of about 400 μm, where a 500 - 600 V voltage is applied. Due to the very high electric field (40 - 50 kV/cm) the electrons produce avalanches with a gain of the order of 104. The thin amplification gap allows a fast ions evacuation, which occurs in about 100 ns, and allows MM to operate in highly irradiated environments.
MM chambers are designed to provide a space resolution below 100 μm and a tracking efficiency better than 95% per single plane. The produced signal is then read by the readout strips capacitively coupled to the resistive ones in order to reduce the performance degradation due to discharges in the detector.
INFN is deeply involved in the Micromegas Chambers construction and testing of the new chambers at the LNF Cosmic Ray Stand. At the LNF an assembly procedure of the chambers to guarantee the alignment of the readout strips has been developed, together with a validation procedure to test the functioning of the detectors.

3.1 Production Scheme

The NSW structure consist of 8 large sectors and 8 small sectors, with 2 modules per sector and 4 MM quadruplets. MM chambers are therefore produced in 4 different shapes: LM1, LM2, SM1, SM2. The production is distributed over different institutes and industries: Germany(SM2), France(LM1), Russia-Greece-CERN (LM2) and Italy is responsible for the SM1 construction. The INFN has been committed to built 32 quadruplets. The INFN Italian production is summarized as shown in Figure 2.

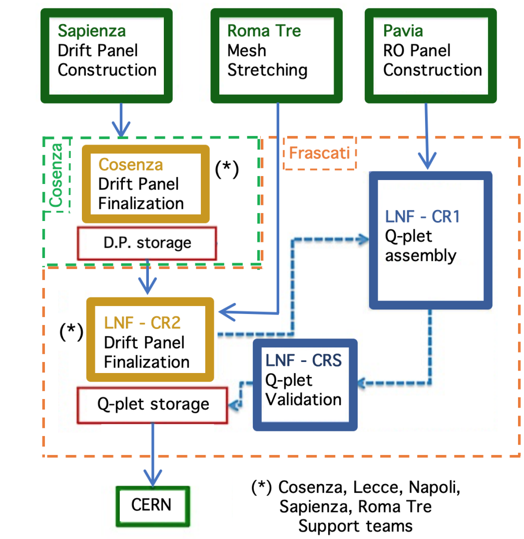

Figure 2: INFN production scheme of SM1.

3.2 HV issue and Passivation Procedure

Due to design issue on the resistive strip layout for the stereo panel (for SM1) and due to the fact that the screenprinting procedure does not give a uniform resistivity among the strips, the Italian group developed a procedure referred to as passivation 3 to protect those weak points. It consists of a layer of glue (araldite 2011) or polyurethan from February 2020 of 120 μ m thickness and variable with to reach a resistance of 0.8 MOhm over a $cm2$ probe from the HV silverline distribution to the pcb.

3.3 Assembly and Validation Procedure

A MicroMegas module is made of four gas gap (*Quadruplet*) and it consists of 5 panels: two outer Drift panels, one central Drift Panel and two Readout panels, the *Eta* (with vertical strip to measure the η coordinate) and the *Stereo* (with strip tilted at $\pm 1.5°$ to measure the ϕ coordinate). A *cleaning procedure* of the panels, using micro-polishing detergent and deionised water, has been developed during this year to remove the most of the contaminants that remain on the panels surface during the production phases and lead to

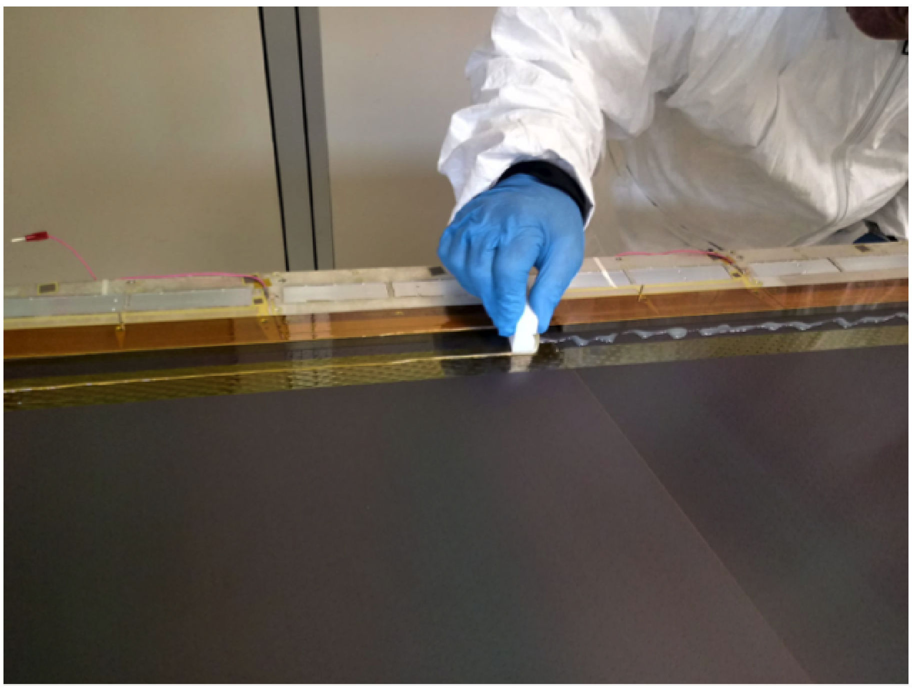

Figure 3: Passivation procedure.

HV issues. The assembly procedure of a module takes place in the clean room, with the use of purpose-built tools to close the module in a vertical way, to reduce the dust deposits and guarantee a good alignment between the two readout panels using load cells. The assembly starts from the closure of the first gap with an outer Drift panel and the Stereo Readout panel and its HV test in air and in $Ar : CO_2$. Then the procedure continues with the assembly of the central Drift, the Eta Readout and the last outer Drift panel. The high voltage test is done on each gap.

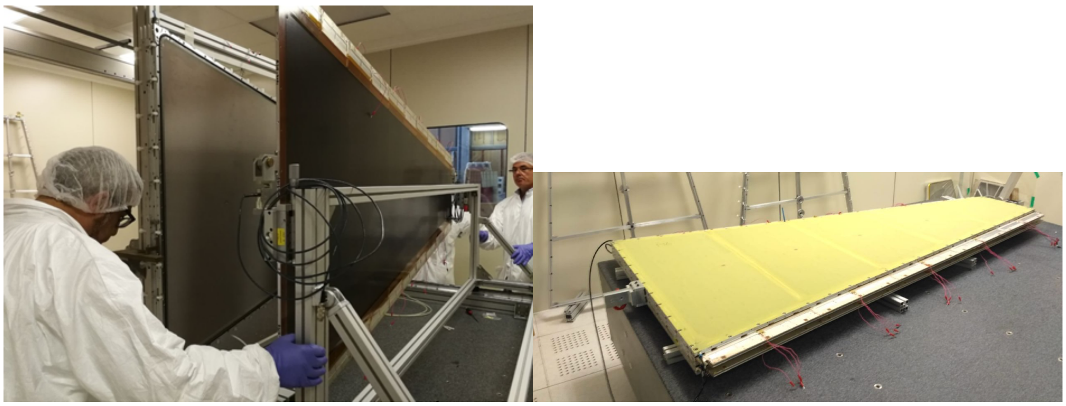

Figure 4: *On the left*: closure of the first gap with the panel positioned on the vertical tools. *On the right*: the assembled quadruplet positioned on the supports ready for the validation measurements in clean room.

At the end of the assembly, when the quadruplet is closed, a series of validation test is done:

- *Planarity and Thickness.* The Quadruplet is positioned on several supports, which represents the reference plane (z=0) for planarity and thickness measurements. All measurements has been made with a Laser Tracker and doing a fit of the cloud points for each side of the quadruplet.
- *Gas Leak Test.* The module is pressurized at ~3 mbar and the pressure drop is monitored to estimate the leak of the chamber.
- *Strip Alignment.* The alignment between the readout-strips of the four layers of the module is measured using the *Double-RasFork*, a tool that reads the coded masks on the side of the PCBs with a contact-CCD installed on it.
- *High Voltage Test.* A slow high voltage *conditioning* procedure is performed for each module. It start applying a voltage of 400 V in the amplification region, and it slowly increases until it reaches the nominal working point for the SM1 module of 570 V.

3.4 Cosmic Ray Stand Test

The modules need to be validated at the Cosmic Ray Stand to estimate the efficiency and the gain uniformity of each chambers.
The experimental setup (Figure 5) currently consists of two scintillators for the trigger coincidence separated by 35 cm of iron, achieving a trigger rate of 50 Hz. The Signals from the read-out strips are read using APV25 front-end readout electronics which provides the collected charge as a function of the time in 25 ns bins. By fitting the risetime of the distribution with an inverse Fermi-Dirac function, the time of the arrival of the signal, defined as the inflection point of the function, and the charge induced on the strip, defined as the maximum of the distribution subtracted by the baseline level, can be measured. For each strip i the time t_i and the charge q_i are therefore measured and clusters are reconstructed as groups of neighboring strips according to dedicated clustering algorithms.
Up to now 14 modules has been produced and fully assembled by the INFN group and we have tested and validated 8 chambers. Two modules has been installed on the first Double-Wedge of the New Small Wheel.

Figure 5: Experimental setup at the ATLAS LNF Cosmic Ray Stand.

3.5 Results of a SM1 module produced by INFN

In this section the results of one of the produced and validated modules are shown. In Figure 6 the planarity plot of the point cloud of one side is shown, in Figure 7 the pressure drop plot is shown, in Figure 8 the scheme of the displacement of the coded masks on the PCBs side, and then of the readout strips, between the Eta and the Stereo readout panel is shown and finally in Figure 9 the plot of the efficiency per Layer are represented.

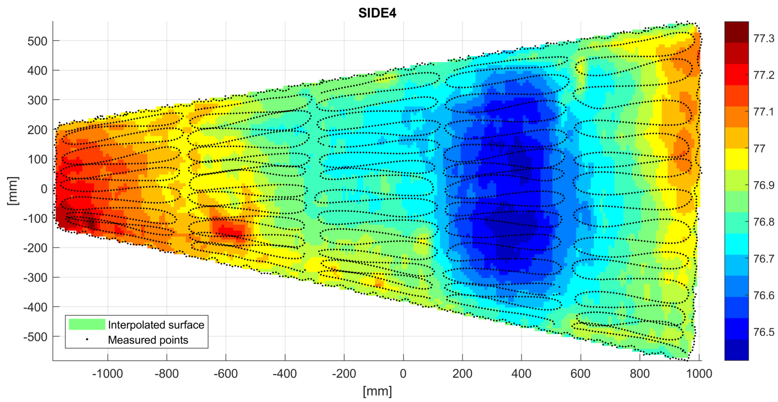

Figure 6: Point cloud obtained with the Laser Tracker on one side of the module for the planarity and thickness measurements.

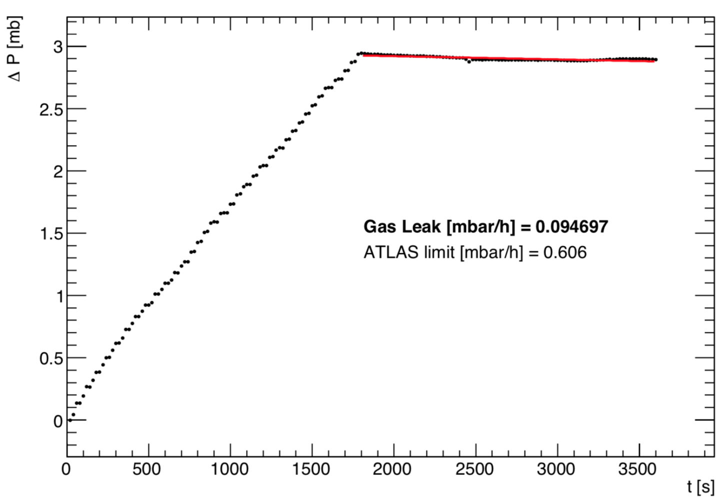

Figure 7: Pressure drop plot to measure the gas tightness of the chamber.

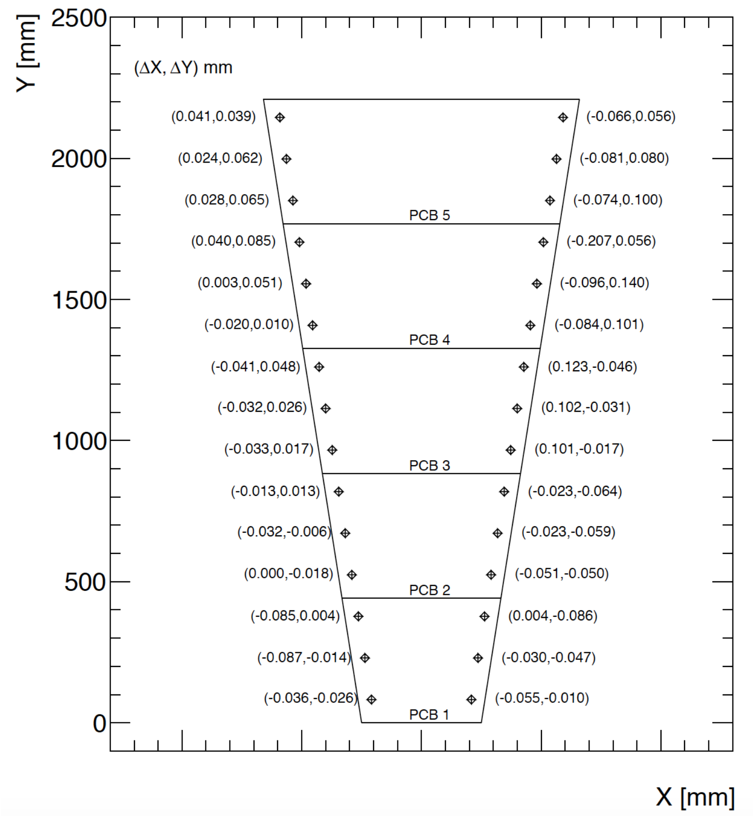

Figure 8: Scheme of the ΔX and ΔY displacement of the readout strips between the Eta and the Stereo readout panel.

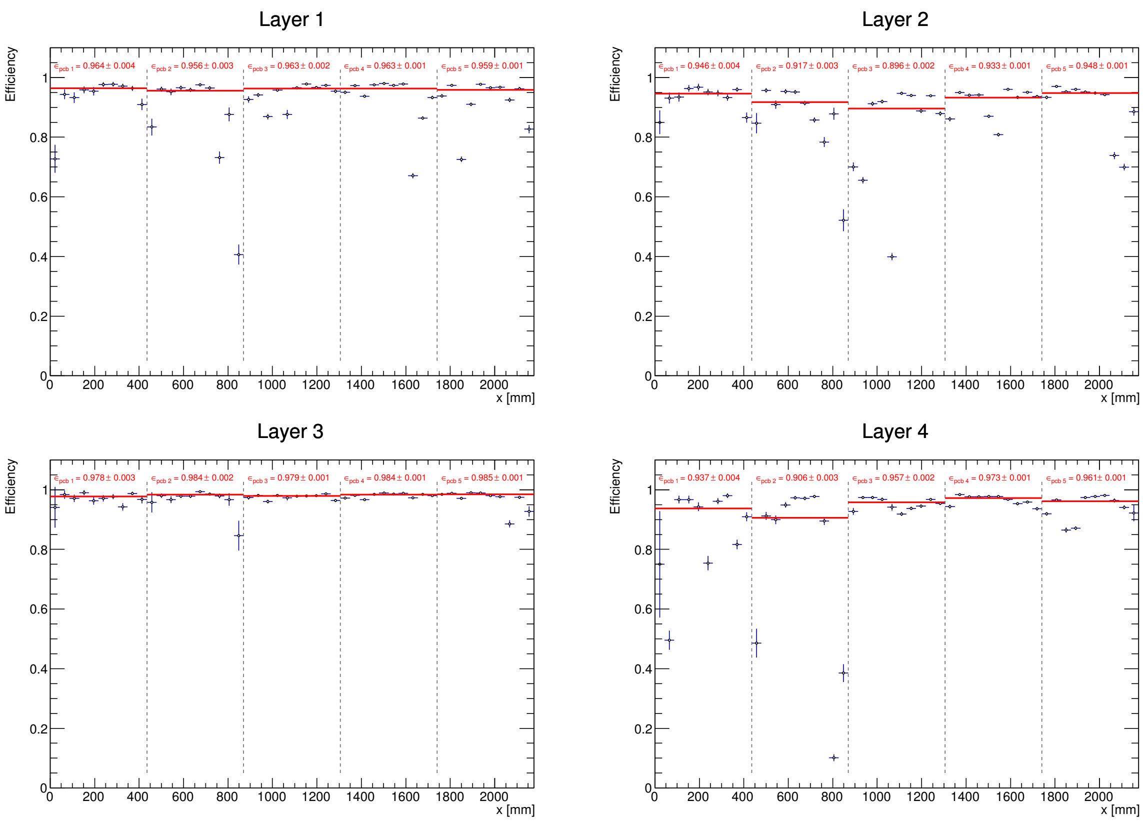

Figure 9: Efficiency plot per Layer.

3.6 Summary of the SM1 chambers produced by the Italian collaboration

In this section the table shows the chambers produced so far together with the overall efficiency of each module 10. It can be noticed that the overall efficiency is increasing with time, i.e. with the introduction of the passivation procedure for the chambers (from M13 on stereo, from M19 on eta panels too). The SM1 chambers presented shows an overall efficiency of $\sim 93\%$.

Chamber	Bad HV sectors (< 560 V)	Mean Efficiency (full chamber)
M6	3	89%
M7	0	95%
M8	4	89%
M9	3	90%
M10	5	90%
M11	3	92%
M12	2	87%
M13	0	96%
M14	1	95%
M15 (660V 80:20)	0	98%
M17	0	96%
M18	3	94%
M19	2	92%
M20	0	95%
M21	0	92%
M22	2	93%
M23	0	95%
M24	0	95%
M25	0	94%
M26	0	96%

Figure 10: Summary of the efficiencies of the SM1 modules built so far by the Italian collaboration.

Responsibilities

- LNF Team: group in charge of the coordination of the production of the MicroMegas chambers for the ATLAS NSW from all the sites: Istituto Nazionale di Fisica Nucleare (INFN), Ludwig Maximilian University of Munich (LMU), Saclay Nuclear Research Centre (CEA), Joint Institute for Nuclear Research of Dubna (JINR), from February 2019.
- M. Antonelli: Production Manager of the MicroMegas production for the NSW for all sites.
- G. Mancini: Responsible of the LNF Cosmic Ray Stand (CRS) for the test and study of the performances of the SM1 MicroMegas (MM) chambers, from September 2017.
- G. Mancini: Responsabile della messa in funzione di un Cosmic Ray Stand presso il CERN per il test e lo studio delle performances delle camere MicroMegas prodotte dall'intera collaborazione per le New Small Wheels (NSWs) di ATLAS, da Ottobre 2019.
- G. Mancini: Convener of the Nuove Tecnologie session for IFAE (Incontri di Fisica delle Alte Energie) 2019, April 2019.
- G. Mancini: Reviewer for MEIE 2020 (Mechanical, Electric and Industrial Engineering).
- G. Mancini: Reviewer for Nuclear Instrumentation Module A.

Public presentations and posters:

- C. Arcangeletti: *Assemblaggio e validazione delle camere MicroMegas SM1 per lupgrade dello spettrometro a muoni dellesperimento ATLAS ad LHC*, IFAE 2019, Incontri di Fisica delle Alte Energie, Napoli (Italy), 8-10 April 2019.
- C. Arcangeletti: *Assemblaggio e validazione delle camere Micromegas per lupgrade dello spettrometro a muoni nella regione in avanti dellesperimento ATLAS*, 105° Congresso Nazionale della Societ Italiana di Fisica, L'Aquila (Italy), 23-27 September 2019.
- G. Mancini: Talk at the MicroPattern Gaseous Detector (MPGD) Conference (La Rochelle) on behalf of the NSW MicroMegas production group: Production of Micromegas and progress on the HV stability issues, 5-10 May 2019.

4 Measurements of the Higgs boson inclusive and differential fiducial cross sections in the $H \rightarrow ZZ^* \rightarrow 4l$ decay channel

The ATLAS detector collected proton-proton collisions at 13 TeV center of mass energy between 2015 and 2018 data taking at LHC, corresponding to an integrated luminosity of $139 fb^{-1}$.
Back on 4 July, 2012, the LHC experiments reported the evidence of an Higgs boson-like particle with a mass of about of 125 GeV and great interest has been posed on the measurements of its properties to assure whether it is the Standard Model (SM) Higgs boson or not. In this context, during the Run2 at LHC, with an increased center of mass energy of the collisions, the measurement of the Higgs properties remains one of the main goals of the physics program since hints of New Physics (NP) effects can be hidden in the Higgs sector. Deviations from the SM expectations could indicate exotic properties of the Higgs or presence of exotic particles in association with Higgs.
The $H \rightarrow ZZ^* \rightarrow 4l$ decay channel is referred to as the *Golden Channel* due to the high signal-background ratio (~ 2) and to a clear signature for the trigger due to the presence of high-p_T leptons that comes from the Z bosons decays. The limit of this decay channel is the low Branching Ratio ($\sim$3%), then it is affected by a lower statistics, but the increase of the integrated luminosity will lead to a lowering of the statistic error on the measurements, because now it is the main contribution on the errors in this channel.
Differential cross sections measurement have been also performed with observables sensitive to the Higgs-boson production and decay modes. These measurements can be used to probe possible effects beyond the SM. Two possible interpretations of the results has been studied. The m_{12} vs. m_{34} double differential cross section is used to probe several BSM scenarios within the framework of the Pseudo-Observables [2] [3]; and the p_T^{4l} differential cross section is used to constrain the Yukawa couplings of the Higgs boson with the light-quarks (b, c) [4].
Our group contributed significantly to this studies ([1]) with fundamental contributions to the analysis and to the interpretation of the results.

4.1 Analysis strategy

The total cross section σ of a process with a given Branching Ratio (BR) ($(1.25 \pm 0.03) \times 10^{-4}$ for the $H \rightarrow ZZ^* \rightarrow 4l$) [5] is defined as:

$$\sigma = \frac{N_s}{\epsilon \cdot BR \cdot L_{int}} \tag{1}$$

where N_s int the number of observed signal events, L_{int} the integrated luminosity and ϵ is the efficiency for detecting the signal process. This efficiency takes into account events which are outside the detector acceptance, then it means that it extrapolates the observed measurements to regions of phase space in which the detector has no sensitivity. It can be split in two terms:

$$\epsilon = A \cdot \epsilon_{fid} \tag{2}$$

where A is the kinematic and geometric acceptance (the model-dependent part) equal to N_{fid}/N_{tot}, the fraction of events that fall within the *fiducial volume* and ϵ_{fid} is the signal reconstruction efficiency within the fiducial volume.
In this way it is possible to define a fiducial cross section:

$$\sigma^{fid} = \sigma \cdot A \cdot BR = \frac{N_s}{\epsilon_{fid} \cdot L_{int}} \tag{3}$$

The fiducial cross sections are defined at particle level using the selection requirements in Figure 11, which are chosen to closely match those in the detector-level analysis after the event reconstruction in order to minimise model-dependent acceptance extrapolations.

	Leptons and jets
Leptons	$p_T > 5$ GeV, $\|\eta\| < 2.7$
Jets	$p_T > 30$ GeV, $\|y\| < 4.4$
remove jets with	$\Delta R(\text{jet}, \ell) < 0.1$
	Lepton selection and pairing
Lepton kinematics	$p_T > 20, 15, 10$ GeV
Leading pair (m_{12})	SFOS lepton pair with smallest $\|m_Z - m_{\ell\ell}\|$
Subleading pair (m_{34})	remaining SFOS lepton pair with smallest $\|m_Z - m_{\ell\ell}\|$
	Event selection (at most one quadruplet per event)
Mass requirements	50 GeV$< m_{12} <$ 106 GeV and 12 GeV$< m_{34} <$ 115 GeV
Lepton separation	$\Delta R(\ell_i, \ell_j) > 0.1$
J/ψ veto	$m(\ell_i, \ell_j) > 5$ GeV for all SFOS lepton pairs
Mass window	105 GeV$< m_{4\ell} <$ 160 GeV
If extra leptons with $p_T > 12$ GeV	Quadruplet with the largest ME

Figure 11: List of event selection requirements which define the fiducial phase space for the cross section measurements.

In general the measurement of a cross section in each bin of a differential distribution, or for each decay final state for the inclusive fiducial cross section, is based on the inclusive signal yield, where the signal extraction is performed fitting the inclusive mass distribution, building a profile likelihood ratio by considering the cross-section as the parameter of interest (POI) with respect the all the others that are considered as nuisance parameters (NPs):

$$\Lambda(m_{4l}|\sigma^{fid}) = \frac{L\left(m_{4l}|\sigma^{fid}, \hat{\hat{\theta}}\right)}{L\left(m_{4l}|\hat{\sigma^{fid}}, \hat{\theta}\right)} \tag{4}$$

The number of expected events N_i in each observable reconstruction bin i, expressed s function of m_{4l} and of the σ^{fid}, is given by:

$$N_i(m_{4l}) = \sum_j \epsilon_{ij}(1 + f_i^{nonfid}) \cdot \sigma_j^{fid} \cdot P(m_{4l}) \cdot L_{int} + N_i^{bkg}(m_{4l}) \tag{5}$$

where $N_i^{bkg}(m_{4l})$ is the background contribution and $P(m_{4l})$ id the m_{4l} signal shape containing the fraction of events expected in each bin. The terms ϵ_{ij} represent the detector response matrix, that correspond to the probability that an event generated within the fiducial volume in the observable bin j is reconstructed in the bin i. Figure 12 shows the migration matrix for p_T^{4l} observable. In this way it is possible to take into account for bin-to-bin migrations in the unfolding. The factor f_i^{nonfid} instead represent the fraction of event that are reconstructed but do not fulfill the fiducial selection criteria.

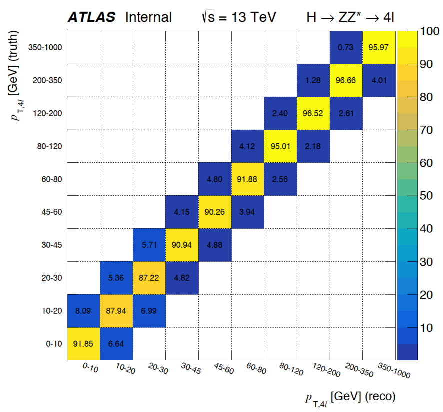

Figure 12: Migration matrix for p_T^{4l}.

4.2 Results

Inclusive and several differential fiducial cross sections are measured [1]. The inclusive cross section results are shown in Figure 13. The differential measurements have been made for variables which show a peculiar sensitivity to the Higgs boson properties. They are reported for the Higgs boson transverse momentum p_T^{4l} and the number of jets N_{jets}, produced in association with the Higgs boson, because this variables can be used to test the SM prediction and constraint beyond SM effects, and they are shown in Figure 14 and Figure 15 together with the correlation matrix.

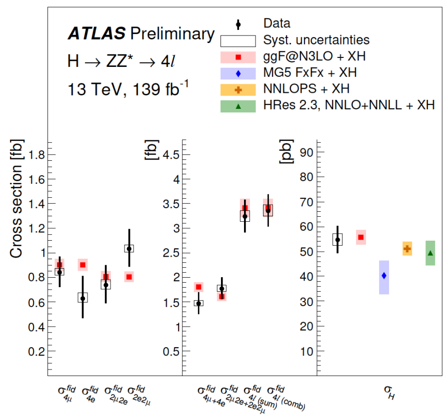

Figure 13: The fiducial cross sections (left two panels) and total cross section (right panel) of the Higgs boson production measured in the $4l$ final state.

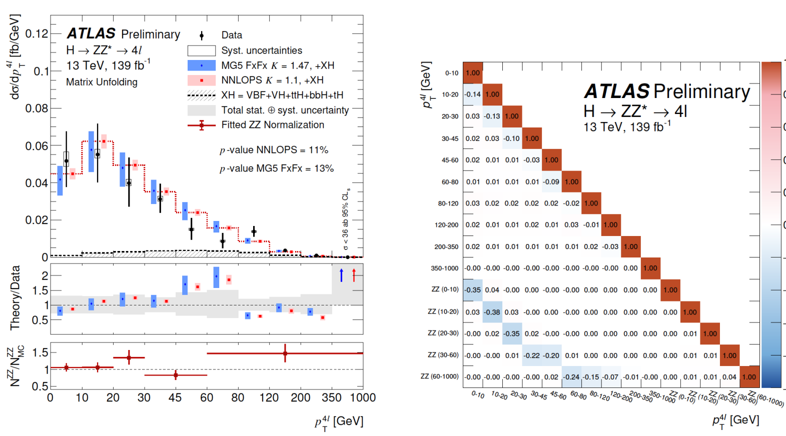

Figure 14: Differential fiducial cross sections for the transverse momentum (*left*) of the Higgs boson, together with the corresponding correlation matrices between the measured cross sections and the ZZ background normalisation factors (*right*) .

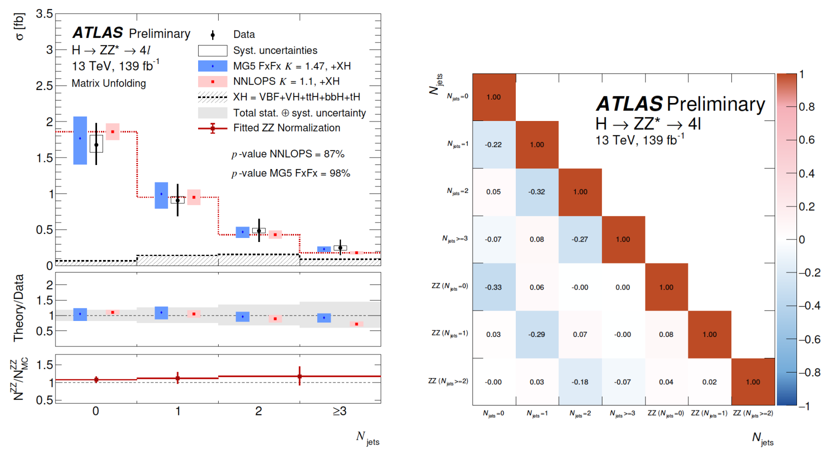

Figure 15: Differential fiducial cross sections for the number of jets (*left*), together with the corresponding correlation matrices between the measured cross sections and the ZZ background normalisation factors (*right*) .

4.3 Interpretation of differential distributions

4.3.1 Pseudo-Observables

In this interpretation, the couplings related to the BSM contact interactions of the Higgs boson decaying into four leptons are considered. These modify the contact terms between the Higgs boson, the Z boson, and the left- or right-handed leptons $\epsilon_{Z\ell(\mathrm{L})}$ and $\epsilon_{Z\ell(\mathrm{R})}$. In order to reduce the number of independent parameters considered in the Pseudo-Observable (PO) framework for the$H \to 4\ell$ decay amplitudes, specific symmetries are imposed. In all the scenarios considered, the parameters associated with other pseudo-observables affecting the angular distributions, such as $\epsilon_{ZZ}^{(CP)}$, $\epsilon_{Z\gamma}^{(CP)}$ and $\epsilon_{\gamma\gamma}^{(CP)}$, are set to zero. Thus, the contact terms considered have the same Lorentz structure as the SM term and only affect the dilepton invariant mass distributions.
The double differential decay distribution in q_1 and q_2 leads to a quadratic polynomial function in k= $(k_{ZZ}, \epsilon_{ZeL}, \epsilon_{Z\mu L}, \epsilon_{ZeR}, \epsilon_{Z\mu R})$, therefore the decay amplitude can be written as a function of the POs as follows:

$$\frac{d^2\Gamma}{dm_{12}dm_{34}} = \sum_{j\geq i} A_{ij} k_i k_j \tag{6}$$

In this analysis the couplings related to the both flavour universal and flavour violating contact-interaction of the Higgs decay are considered as outlined in [6]. The scenarios considered are:

- **Linear EFT-inspired:** $(\kappa_{ZZ}$ vs. $\epsilon_{Z\ell(\mathrm{R})})$, where $\epsilon_{Z\ell(\mathrm{L})} = 0.48\epsilon_{Z\ell(\mathrm{R})}$, $\epsilon_{Ze(\mathrm{R,L})} = \epsilon_{Z\mu(\mathrm{R,L})}$ and other $\epsilon \to 0$.

- **Flavor universal contact terms:** ($\epsilon_{Z(\mathrm{R})}$ vs. $\epsilon_{Z(\mathrm{L})}$): where $\epsilon_{Ze(\mathrm{L})} = \epsilon_{Z\mu(\mathrm{L})}$, $\epsilon_{Ze(\mathrm{R})} = \epsilon_{Z\mu(\mathrm{R})}$, $\kappa_{ZZ} = 1$ and other $\epsilon \to 0$.
- **Flavor non-universal vector contact terms:** ($\epsilon_{Ze(\mathrm{R})}$ vs. $\epsilon_{Z\mu(\mathrm{R})}$), where $\epsilon_{Ze(\mathrm{L})} = \epsilon_{Ze(\mathrm{R})}$, $\epsilon_{Z\mu(\mathrm{L})} = \epsilon_{Z\mu(\mathrm{R})}$, $\kappa_{ZZ} = 1$ and other $\epsilon \to 0$.
- **Flavor non-universal axial contact terms:** ($\epsilon_{Ze(\mathrm{R})}$ vs. $\epsilon_{Z\mu(\mathrm{R})}$), where $\epsilon_{Z\ell(\mathrm{L})} = -\epsilon_{Z\ell(\mathrm{R})}$, $\kappa_{ZZ} = 1$ and other $\epsilon \to 0$.

The contact terms have the same Lorentz structure as the SM term, therefore, the angular distributions are not modified and the contact terms only affect the dilepton invariant mass spectra. The unfolded observable that is sensitive to modifications from new physics is m_{12} versus m_{34}. Other pseudo-observables affecting the angular distributions, such as $\epsilon_{ZZ}^{(CP)}$, $\epsilon_{Z\gamma}^{(CP)}$ and $\epsilon_{\gamma\gamma}^{(CP)}$, are not considered in this analysis. Assuming the SM values for all but the tested parameters, limits are set on the contact-interaction coupling strength.

Strategy The same strategy is followed for each of these interpretations. The cross-section in each bin of m_{12} versus m_{34} distribution is calculated by simulating a grid of couplings values for the given parameters.
The calculated acceptance in each bin is multiplied by the predicted cross-section, and further normalized to the predicted cross-section when all couplings are fixed to their SM value. These values are fit with a 2D quadratic function in the inclusive final state for Linear EFT-inspired and universal contact terms interpretations, and are they are fit in $\ell\ell ee$ and $\ell\ell\mu\mu$ final states for the non-universal lepton interpretations. The re-parametrizations of the cross sections are incorporated into the likelihood and exclusions limits are derived.
To check the validity of the parameterization, the additional points are generated around the expected 68% and 95% limits. For these, the expected exclusion is calculated using the parametrized function and the unfolded results. For all interpretations, the difference between the two methods is $< 5\%$.
The impact of the systematics has been investigated by varying the renormalization and factorization scale in Madgraph. These variation are the same across all coupling values across all bins sensitive to modification. These systematics modify the production modes therefore we can apply this as a flat systematic for each bin of m_{12} versus m_{34}. However, as the MC is at NLO accuracy, the derived scale variation are significantly large. Instead, we choose to apply the Higgs systematics recommended by the LHCXSWG as the theoretical uncertainty as they are calculated at a higher order and have an approximately 5% impact across the mass spectrum.

Expected Results The expected exclusion plots are shown in Figure 16.

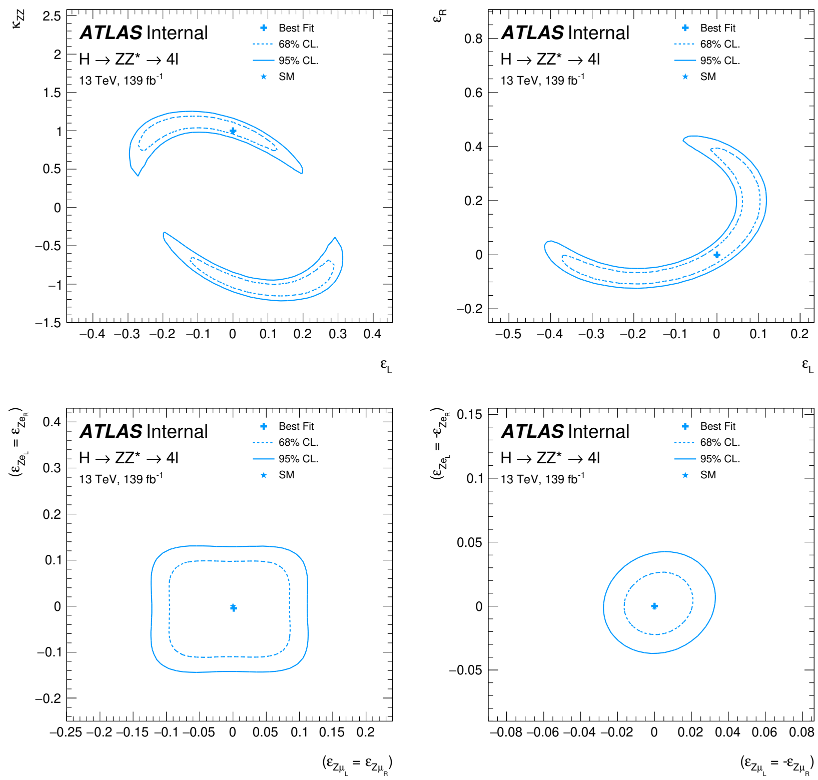

Figure 16: Expected exclusions for all the scenarios: k_{ZZ}, ε_L (*top-left*); $\varepsilon_L, \varepsilon_R$ (*top-right*); $\varepsilon_\mu, \varepsilon_e$ (*bottom-left*); $\varepsilon_{\mu R}, \varepsilon_{eR}$ (*bottom-right*).

4.3.2 Light-Yukawa

The coupling of the Higgs boson to the top and bottom quark have been previously measured. Measuring the coupling of the Higgs boson to lighter generation quarks, such as the charm quark, has been much more difficult due to small branching fractions in channels that can probe it well ($h \to J/\psi\gamma \to \mu^+\mu^-$) or large QCD backgrounds ($VH(\to c\bar{c})$). However, it was recently proposed that the coupling can be constrained with current LHC data by analyzing modifications to the p_T^H shape. For this interpretation three scenarios has been considered:

- The cross section and p_T^H shape can be modified
- The cross section and p_T^H shape and branching ratio can be modified
- The cross section is fixed to the SM but the p_T^H shape can be modified

In the interpretation κ_B is simultaneous fit alongside κ_C. This is so that any large deviations from lighter generation charge = -1/3 quarks can be seen from κ_B.

Strategy This interpretation follows the same strategy as pseudo-observables.The cross section is parametrized as a function of κ_B and κ_C values in each bin of p_T^H.
Theory systematics are considered separately for gluon and quark initiated processes. For gluon initiated processes, variations in the renormalization, factorization and matching scale are considered. The largest up and down variation across all κ_B and κ_C values is taken and applied as a flat systematic for each p_T^H bin. For quark initiated processes the normalization and factorization scale are varied in an 8-point variation. Again, the largest variation across all κ_B and κ_C is applied as a flat systematic for each p_T^H bin. Approximately, a 20% impact is observed in the expected limits.

Expected Results The 2D expected exclusion plots are shown in Figure 17 for the different scenarios and the 1D expected results with κ_B held to 1 are shown in Figure 18.

Public presentations and posters:

- G.Mancini, *ATLAS H(125) boson decays results*, Talk at Higgs Hunting Paris 2019 on behalf of the ATLAS Collaboration, 29-31 July 2019.

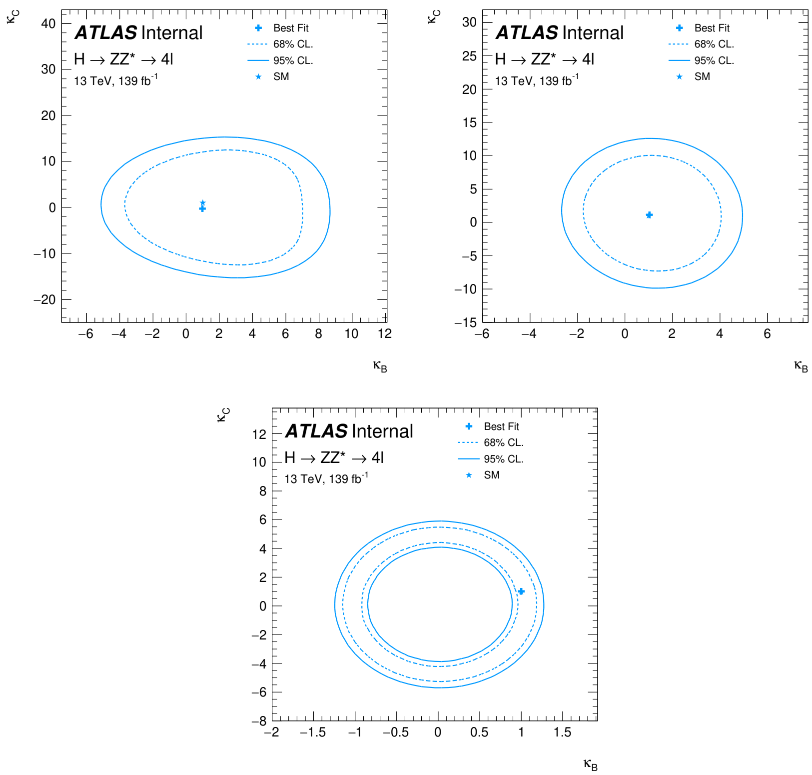

Figure 17: Expected exclusions for all the scenarios: only the p_T^{4l} shape is used to constraint κ_B and κ_C (*top-left*); the predicted p_T^{4l} differential cross section is used (*top-right*); both the prediction of the p_T^{4l} differential cross section and the modification to the branching ratio due to the κ_B and κ_C values are used (*bottom*).

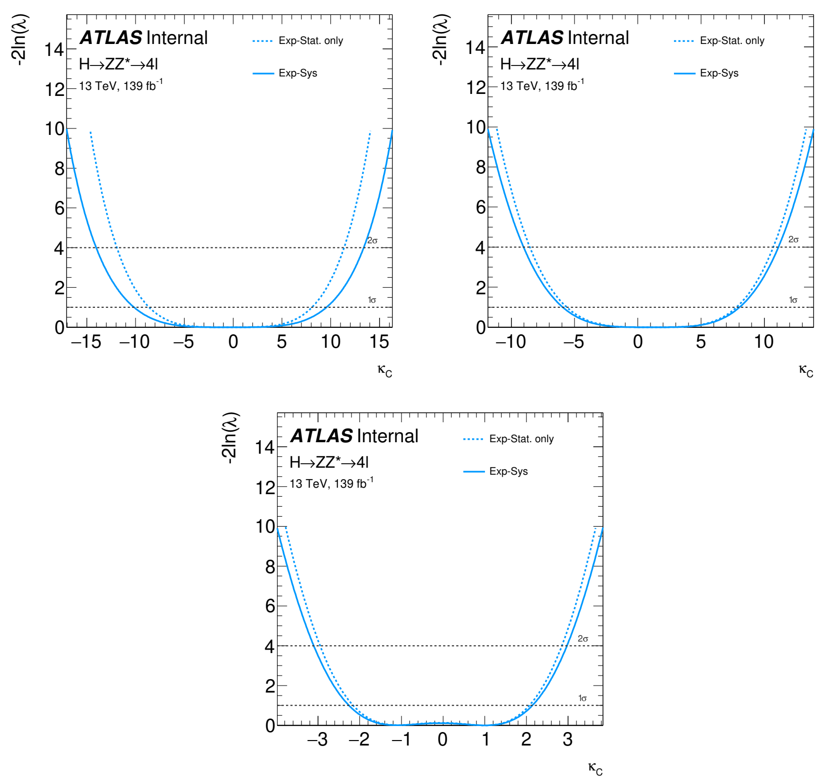

Figure 18: 1D expected results for all the scenarios: only the p_T^{4l} shape is used to constraint κ_B and κ_C (*top-left*); the predicted p_T^{4l} differential cross section is used (*top-right*); both the prediction of the p_T^{4l} differential cross section and the modification to the branching ratio due to the κ_B and κ_C values are used (*bottom*).

5 Inner Tracker (ITk) for Phase-II upgrade

After the “Phase-I” upgrade in 2018, the LHC will undergo a “Phase-II” upgrade in 2023, to deliver the instantaneous luminosity of $\sim 7.5 \times 10^{34} cm^{-2} s^{-1}$, more than a factor 10 beyond its design value, corresponding to unprecedented pile-up conditions with an a average of 200 interactions per crossing. The ATLAS detector will be upgraded to maintain its capabilities. In particular the Inner Detector, with acceptance up to $|\eta| < 2.5$, will be substituted by a new, all-silicon Inner Tracker (ITk), whose acceptance will be $|\eta| < 4.0$. The ITk detector comprises two subsystems: a Strip Detector surrounding a Pixel Detector. The ITk layout is shown in Fig.19, left. The Strip Detector (blue), covering $|\eta| <2.7$, is complemented by a 5 layer Pixel Detector (red) extending the coverage to $|\eta| < 4$. LNF is involved in the construction of one outer pixel endcap of the ITk and in simulation of the performance of the reconstruction of jets and the missing transverse energy.

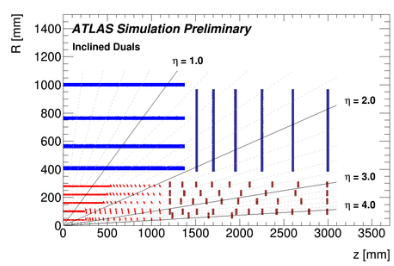

Figure 19: Schematic layout of the ITk. The barrel and endcap for the pixel and strip sub-systems are shown in red and blue respectively. The rings of the pixel endcap are shown as red vertical lines.

5.1 ITk outer-endcap construction

LNF is responsible of the construction of one outer endcap of the ITk Pixel detector. The pixel end-cap system is designed to supply a minimum of at least 9 hits from the end of the strip coverage in pseudorapidity to $|\eta| = 4$. The novel concept is the end-cap ring system, where layers of pixel rings extend the coverage in z and allow routing of the service separately along each ring layer. Each ring can be individually placed to optimize the coverage. More information are in [10]. A 3d model of one outer endcap is shown in Fig.20, left. Each layer of rings is supported by a 0.4mm carbon fiber cylinder shell, along which services for the rings are routed. Each ring is constructed from two half-rings, each covering just over half of the ϕ coverage of the entire ring (Fig.20, right). The two half rings in a pair are separated in z by 10 mm, to allow them to overlap in ϕ such that each ring is hermetic for $p_{\mathrm{T}} = 1$ GeV

primary particles. The pixel services (cables, cooling pipes, data lines) are routed from their sources out to Pixel Patch-Panel 1 (PP1). LNF is responsible of the design, prototyping and construction of the PP1, and of the endcap prototype design and construction. The design of the prototype of the endcap and the PP1 is shown in Fig.21. The bid for the construction of the PP1 and endcap prototypes was completed last year. The 90% of the PP1 prototype construction is scheduled by end of March. The rest of the PP1 prototype and the endcap prototype will be completed once the details on the interface with the Pixel Support Tube and Inner Support Tube will be defined. A crucial part of the PP1 design is the data cable feed-through. A full scale prototype has been realized and filled with Araldite glue. Leak rate measurements are on going. Gaskets resistant to hard radiation have been ordered and will be exposed to 300 Mrad at CERN.
The design of the tools needed for the endcap assembly has started this year. A preliminary design of these tools to insert the half-rings into the shells and that for the clamping of the two half shells is shown in Fig. 22. The tools to hold and transport the endcap should be compatible with the integration at CERN of the endcaps with the barrel. The sequence of integration has been defined in November 2019.
The quality control during the assembly has been studied and defined. Thermal cycling of the loaded half-shells from -45C to +50 is foreseen for the quality control. For the quality assurance, a thermal cycle from -55C to +60 is foreseen on a full-z half-shell prototype populated with services and half-rings. A large climate chamber is foreseen to be purchased by LNF for these tests. Specifications and technical details for the bid are on going.

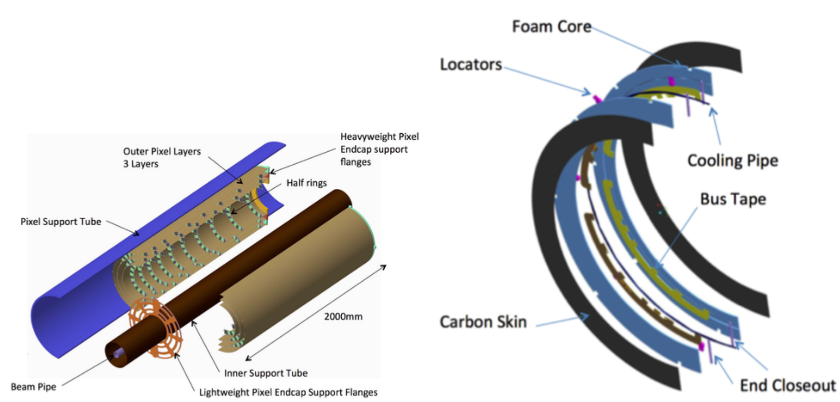

Figure 20: Left: Exploded 3D drawing of one Outer End-cap. Right: Exploded view of the surface of a half-ring

During the construction phase, a CO_2 cooling system will cool-down modules to $\sim$ -20C, through the cooling pipes inside the half-rings. This large CO_2 cooling system is currently in construction in collaboration with CERN and

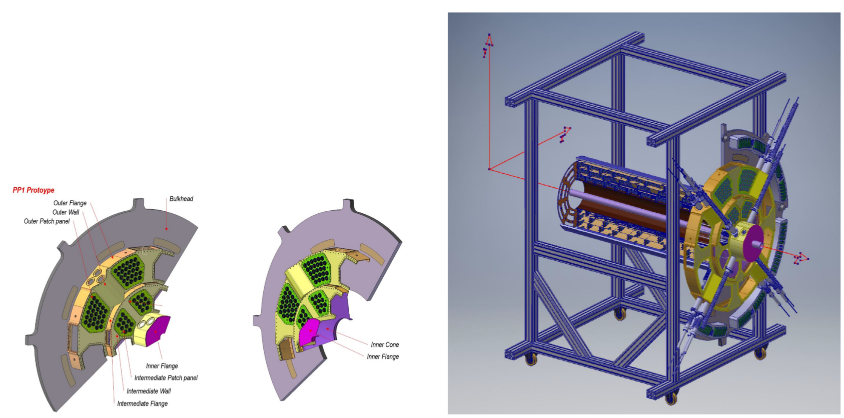

Figure 21: Left: design of the PP1 prototype. Right: design of the endcap prototype.

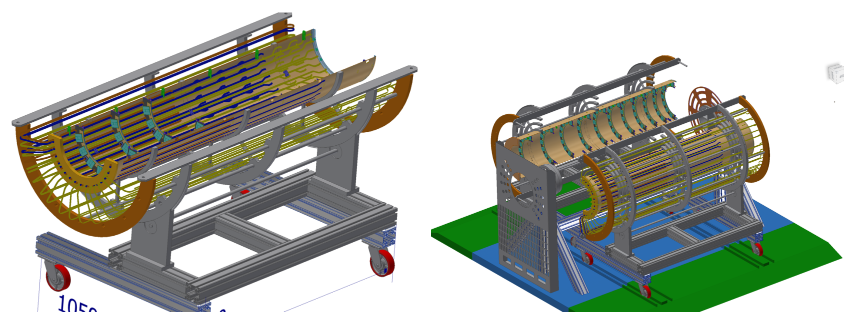

Figure 22: Left: design of tools for half-ring insertion into the shell. Right: design of the tools to clamp two shells.

DESY and NIKHEF institutions.
A project for the refurbishment of the clean room inside Capannone Gran Sasso has been proposed and the executive project is on going.
Publications, internal documents and public presentations:

- S. Tomassini, “Leak Rate Specification for the Pixels PP1”, AT2-IP-ES-0008, in progress
- several presentations during the ATLAS Upgrade week and ITk week at CERN

Responsibilities in ATLAS

- Responsibility for one pixel endcap integration
- Responsibility of the design and construction of two “patch panels 1”

5.2 Jet/E_{T}^{miss} offline reconstruction performance

There is tremendous potential for improved performance for jets and $\not{E}_T$ in the very forward region. Tracking information can be used by tagging pile-up jets in the forward region as has been done in the central region for Run I and Run II. Forward pile-up jets rejection induces an improvement in $\not{E}_T$ as well. The variable used to study the forward pile-up jet tagging is $R_{pT} = \frac{\Sigma_k p_T^{trk_k}(PV_0)}{p_T^{jet}}$ which computes the scalar sum of the p_T of the charged tracks associated with a particular jet, which are also associated with the primary vertex (PV0), and normalizes this to the p_T of the relevant jet. The rejection of pile-up jets versus the efficiency of the R_{pT} cut for hard-scatter jets is shown in Figure 23, left. These results contributed to the coiche of the pixel size which was taken in 2019. The $\not{E}_T$ resolution as a function of the local pile-up density is shown in Figure 23, right. More information is in [10].

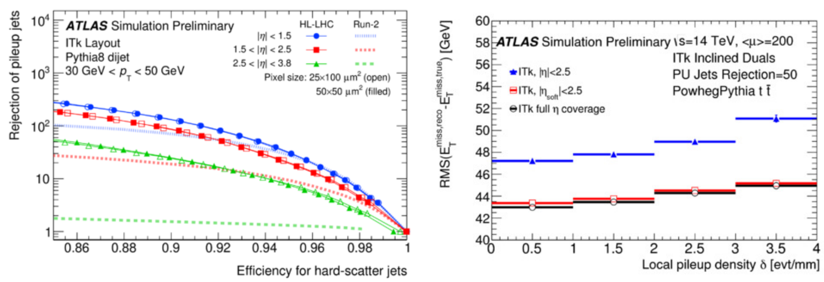

;

Figure 23: Left: The rejection of pile-up jets as a function of the efficiency for hard-scatter jets with $30 < pT < 50$ GeV p_T using the R_{pT} discriminant in di-jet events with an average of 200 pile-up events. Right: The resolution of $\not{E}_T$ in Monte Carlo $t\bar{t}$ events with an average of 200 pile-up events as a function of the local pile-up vertex density around the hard-scattering vertex, for three different $\not{E}_T$ definitions. The first (blue) considers only tracks in the region $|\eta| < 2.5$ for both pile-up jet rejection and soft-tracks not belonging to jets. The second uses tracks for pile-up jet rejection up to $|\eta|$ of 4 (red). The third uses tracks for pile-up jet rejection and soft-tracks up to $|\eta|$ of 4 (black).

5.3 Jet online Reconstruction performance

In the baseline TDAQ architecture at HL-LHC the Level-0 (L0) Trigger output rate is limited to 1 MHz (fully based on calorimeter and muon information) and the output rate to storage is 10 kHz. An evolved TDAQ architecture is also considered, where the detectors are read out at a 4 MHz L0 rate. The Level-1 (L1) Track Trigger provides reconstructed tracks which, combined with calorimeter and muon information, allow for further rejection down to 600 kHz. The output rate to storage remains 10 kHz. More information can be found in [11]. One of the key goals of the L1 Track Trigger is the pile-up mitigation in hadronic trigger selections. However only a limited number of pixel layers can be read out. Three scenarios have been considered: the "MoU", the "TDR" and the "Pix 3L" scenarios. The pixel layers and coverage used in these scenarios are shown in Fig. 24, left. The performance of rejecting pile-up jets in these scenarios are shown in Fig. 24, right. The R_{pT} discriminant considered in the previous section is used. A decision on the number of pixel layers to be read at the L1 Track Trigger will happen in the coming year.

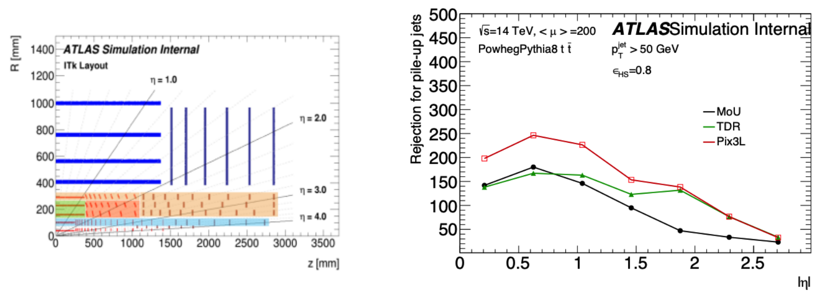

Figure 24: Left: The scenarios considered in the evaluation of the jet performances: the MoU case shown in orange; the TDR case shown in orange plus red; the PIX 3L case shown with the addition of green. Right: The rejection of pile-up jets as a function of $|\eta|$, assuming 80% efficiency for jets coming from the primary vertex

Responsibilities in ATLAS

- Responsibility for the data quality of the offline reconstruction of Missing Transverse Energy (2015-present)
- Convener of the Higgs Prospects analysis group (April 2017 - present)

Publications, internal documents and public presentations:

- ATLAS Collaboration,"Tracking Performance of the ITk", ATL-PHYS-PUB-2019-014
- ATLAS Collaboration, "Expected performance at HL-LHC", ATL-PHYS-PUB-2019-005
- A. Sfyrla, E. Lipeles, S. Majewski, E. Bros, M.Testa et al, "Pixel regional read-out: impact on trigger selections", https://cds.cern.ch/record/2706965/files/ATL-COM-DAQ-2020-007.pdf
- M. Testa, Invited talk "HL-LHC Higgs Physics" at Workshop on the Circular Electron-Positron Collider, EU Edition 2019, 15-17 April 2019

- ATLAS Collaboration, “ATLAS data quality operations and performance for 2015-2018 data-taking”, arXiv:1911.04632, will appear in JINS
- ATLAS Collaboration “Search for light long-lived neutral particles produced in pp collisions at $\sqrt{s} = 13$ TeV and decaying into collimated leptons or light hadrons with the ATLAS detector”, will appear in EPJC, arXiv:1909.01246

References

[1] ATLAS Collaboration, *Measurement of the Higgs boson inclusive, differential and production cross sections in the $4l$ decay channel at $\sqrt{s}$=13 TeV with the ATLAS detector* (ATLAS-CONF-2019-025, July 15, 2019)

[2] M. Gonzalez-Alonso, A. Greljo, G. Isidori and D. Marzocca, *Pseudo-observables in Higgs decays*, Eur. Phys. J. C75 (2015) 128

[3] M. Gonzalez-Alonso, A. Greljo, G. Isidori and D. Marzocca, *Electroweak bounds on Higgs pseudo-observables and $h \to 4l$ decays*, Eur. Phys. J. C75 (2015) 341

[4] F. Bishara, U. Haisch, P. F. Monni, and E. Re, *Constraining Light-Quark Yukawa Couplings from Higgs Distributions*, Phys. Rev. Lett. 118 (2017) 121801

[5] LHC Higgs Cross Section Working Group (S.Dittmaier et al.), *Handbook of LHC Higgs Cross Sections: 1. Inclusive Observables*, CERN-2011-002 (2011)

[6] Gainer, J.S., Gonzlez-Alonso, M., Greljo, A. et al., *Adding Pseudo-Observables to the Four-Lepton Experimentalist's Toolbox*, J. High Energ. Phys. (2018) 2018: 73.

[7] ATLAS Collaboration, *ATLAS New Small Wheel: Technical Design Report*, Technical Design Report ATLAS. CERN-LHCC-2013-006. CERN, Geneva, 2013

[8] Y. Giomataris et al., *MICROMEGAS: a high-granularity position-sensitive gaseous detector for high particle-flux environments*, Nucl. Instrum. Meth. A 376 29, 1996

[9] M. Iodice [ATLAS Muon Collaboration], *Micromegas detectors for the Muon Spectrometer upgrade of the ATLAS experiment*, JINST 10 (2015) no.02, C02026;

[10] ATLAS Collaboration, “Technical Design Report for the ATLAS ITk Pixel Detector”, CERN-LHCC-2017-021; ATLAS-TDR-030

[11] ATLAS Collaboration, “ATLAS Trigger and Data Acquisition Phase-II Upgrade Technical Design Report”, CERN-LHCC-2017-020; ATLAS-TDR-029